

Rational Control of Magnonic and Electronic Band Splittings

Subhadeep Bandyopadhyay,^{1,2} Anoop Raj,³ Philippe Ghosez,¹ Sumiran Pujari,³ and Sayantika Bhowal^{3,*}

¹*Theoretical Materials Physics, Q-MAT, Université de Liège, B-4000 Sart-Tilman, Belgium*

²*Consiglio Nazionale delle Ricerche (CNR-SPIN), Unità di Ricerca presso Terzo di Chieti, c/o Università G. D'Annunzio, I-66100 Chieti, Italy*

³*Department of Physics, Indian Institute of Technology Bombay, Mumbai 400076, India*

(Dated: September 11, 2025)

We provide a theoretical demonstration of controllable non-relativistic spin splitting in both electronic and magnonic bands via targeted structural distortions tied to specific phonon modes. Using MnF_2 as a model system, we identify a d -wave magnon band splitting between magnon modes of specific handedness, directly correlated with the non-relativistic spin splitting observed in the electronic structure. Crucially, we show that structural distortions associated with the A_{2u} and A_{1g} phonon modes (8.52 and 9.74 THz) modulate these splittings without altering the antiferromagnetic order. The effect originates from changes in the nonmagnetic ligand environment, highlighting the key role of lattice degrees of freedom in governing spin dynamics. Our findings establish a novel route for structure-mediated control of spin splitting, opening possibilities for tunable magnonic and spintronic functionalities in antiferromagnetic materials.

Splitting between spin-polarized bands of antiferromagnets has recently been at the center of attention. Such spin-split antiferromagnets (SSAFMs), also known as “altermagnets”, are distinguished by significant spin splitting in momentum space, even without spin-orbit coupling (SOC) or net magnetization [1–17]. By combining traits of ferromagnets and conventional antiferromagnets (AFMs), SSAFMs offer new possibilities for achieving otherwise difficult properties, such as efficient spin-current generation [18–22], spin-splitting torque [23, 24], giant magnetoresistance [25], spontaneous Hall effect [14, 26–32] without any magnetization as well as unconventional superconducting properties [33–38], and enhanced thermal transport [39, 40].

Recent theoretical predictions [41, 42], now confirmed by inelastic neutron scattering experiments [43], suggest that magnon bands in SSAFMs exhibit similar splitting to electronic bands, resulting in non-degenerate magnon modes with specific handedness, referred to as “chiral” magnons [41]. The handedness can be thought of in analogy with the polarization of photons as quanta of electromagnetic vector fields, since magnons are quanta of waves made out of electron spins, which are also vectorial in nature [44]. This development brings us closer to realizing advanced magnonic devices that rely on magnon-generated spin currents in AFMs, functioning without the need for external magnetic fields to generate the splitting [45].

In this work, we show the control of splitting in spin-polarized electronic and magnonic bands by controlling the structural distortion associated with specific phonon modes with frequencies in the terahertz (THz) regime without changing the AFM order. We illustrate our findings using MnF_2 as a representative material for SSAFMs. Our interest in MnF_2 stems from recent dis-

coveries in this nearly century-old material [46–48], which highlight unusual spin splitting [2], the presence of ferroic ordering of higher-order magnetic octupoles [49, 50], and ongoing efforts [51–54] to manipulate its magnetism via structural modifications.

Our key findings are threefold. First, we demonstrate that the magnon bands in MnF_2 exhibit a d -wave splitting, similar to its electronic bands. We identify the wave vector where not only is the splitting maximum, but also the magnon bands possess a pure left and right-handedness, which can be crucial for detection using polarized neutron or X-ray scattering techniques. Second, we identify structural distortions that are related to two stable Γ -point phonon modes in MnF_2 and show that by jointly controlling these distortions, it is possible to manipulate the energy splitting between the magnon bands. In practice, such structural control can be achieved, for example, using an external electric field, optical pulses, or strain engineering. Third, we reveal a striking correlation between electronic and magnonic bands, enabling the control of spin splitting in the electronic bands, leading to a transition from SSAFM to a conventional AFM with no spin splitting.

Our work advances the current understanding of the interplay between structural geometry and magnetism in SSAFMs. We go beyond symmetry considerations to show that the local geometry of nonmagnetic ligand atoms plays a crucial role in inducing anisotropic magnetization density in the ground state, leading to direction-dependent exchange coupling between magnetic atoms. While the anisotropic magnetization density, characterized by ferroic magnetic octupoles [49], is essential for spin splitting in electronic bands, we analytically demonstrate that magnon band splitting arises from the direction-dependent exchange coupling. Thus, by tuning the positions of nonmagnetic ligand atoms following specific phonon modes, we can simultaneously control the electronic and magnonic spin splittings.

* sbhowal@iitb.ac.in

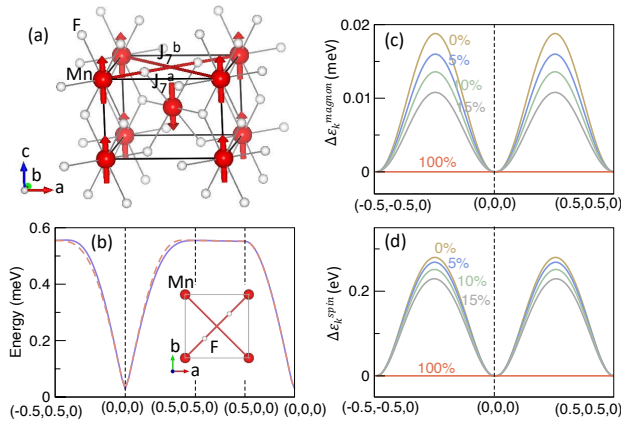


FIG. 1. Control of magnon and electronic spin splitting in MnF_2 by tuning A_{2u} and A_{1g} distortions jointly. (a) Crystal structure of MnF_2 , indicating the Mn ions on the ab plane corresponding to the J_7 exchange coupling. The bonds indicate the Mn-Mn interaction paths along $[110]$ (J_7^a) and $[\bar{1}\bar{1}0]$ (J_7^b) directions with and without the F ions sitting in between, respectively. The arrows indicate the direction of the Mn spin moments in the ground state of MnF_2 . (b) Computed magnon spectrum of MnF_2 . The γ_k term, identical for both branches, has been scaled by a factor of 0.1 to make the splitting more apparent. The inset shows the $z = 0$ plane of MnF_2 , highlighting the presence and absence of F-ions along the J_7^a and J_7^b exchange paths. (c) The variation in magnon splitting as a function of combined distortion of phonon modes, A_{2u} and A_{1g} , along specific directions in the momentum space. (d) The corresponding NRSS in the electronic band structure for the second-most top pairs of valence bands along the same k path for different amplitudes of the distortions.

Our work takes a new step in the direction of the recent efforts [55–57] to control non-relativistic spin splitting (NRSS) by introducing a universal approach that extends beyond (anti-) ferroelectric materials. We show that NRSS can be tuned by manipulating the ligand ion environment through specific structural phonon mode distortions. This phonon-assisted control also opens a pathway for ultrafast manipulation of next-generation magnonic devices [58].

Magnon spectra in MnF_2 . We begin by demonstrating the magnon band splitting in MnF_2 . MnF_2 crystallizes in the rutile structure ($P4_2/mnm$) (see Fig. 1a), with spin moments aligned along the $[001]$ direction and antiparallel between Mn ions [46–48]. This magnetic ordering breaks global time-reversal symmetry (\mathcal{T}), resulting in spin splitting in the ground state electronic band structure [2, 49]. To investigate whether the magnon bands exhibit a similar splitting, we first construct the relevant spin model by calculating the Heisenberg exchange interactions between Mn^{2+} ions ($S = 5/2$). These interactions are computed by mapping the total energy obtained from DFT+ U [59–62] calculations to a Heisenberg spin model for four different collinear magnetic configurations [63–65].

Our computed exchange interactions (J_i) up to the seventh nearest neighbors (NNs) ($i = 1, 7$) [See Figs. 1 and 2 of the Supplemental Materials (SM) [65]] show that the magnitude of the intra-sublattice coupling J_7 , corresponding to the seventh NN Mn-Mn distance ($d_7 = 7.03$ Å), varies with direction ($[110]$ vs. $[\bar{1}\bar{1}0]$). This direction-dependent exchange interaction arises from the crystal geometry. As illustrated in Fig. 1a and the inset of Fig. 1b, two F atoms at $(x, x, 0)$ and $(-x, -x, 0)$ [or $(-x + \frac{1}{2}, x + \frac{1}{2}, \frac{1}{2})$ and $(x + \frac{1}{2}, -x + \frac{1}{2}, \frac{1}{2})$] lie along the $[110]$ ($[\bar{1}\bar{1}0]$) direction, but not along $[\bar{1}\bar{1}0]$ ($[110]$), of the J_7 exchange path connecting the corner (central) Mn ions. This leads to stronger coupling along the former and weaker coupling along the latter. We refer to these exchange couplings as J_7^a and J_7^b , respectively. A similar direction-dependent exchange has been reported for the iso-structural compound RuO_2 [41]. However, the further-neighbor coupling J_7 in MnF_2 is much weaker than in RuO_2 , likely due to the itinerant magnetism considered in the latter [41, 66–69].

We further compute the uniaxial single-ion anisotropy D_c from the energy difference between AFM configurations with spins along \hat{x} and \hat{z} in the presence of SOC. Using the computed exchange couplings J_{ij} (up to 7th NN) and D_c , we construct the spin Hamiltonian for MnF_2 , $\mathcal{H}_{\text{spin}} = \sum_{ij} J_{ij} \vec{S}_i \cdot \vec{S}_j + \sum_i D_c (S_i^z)^2$. Through analytical spin-wave calculations, using the Holstein-Primakoff transformation [70] and the Fourier transformation, we obtain the Hamiltonian in terms of the bosonic operators a_k and b_k in the reciprocal space as

$$H_k = \sum_k [A_k a_k^\dagger a_k + B_k b_k^\dagger b_k + C_k a_k b_{-k} + C_k^* a_k^\dagger b_{-k}^\dagger] \quad (1)$$

Here, a_k (a_k^\dagger) and b_k (b_k^\dagger) are the Fourier transforms of the bosonic operators a_i (a_i^\dagger) and b_i (b_i^\dagger), respectively. The functions A_k , B_k , and C_k are periodic in momentum \vec{k} and explicitly depend on the exchange parameters J_i (see SM [65] for details). We then diagonalize the Hamiltonian using Bogoliubov transformation. The resulting Hamiltonian in terms of the magnon operators of α and β modes reads as:

$$H_k = \sum_k [\epsilon_\alpha(k) \alpha_k^\dagger \alpha_k + \epsilon_\beta(k) \beta_k^\dagger \beta_k]. \quad (2)$$

Here, $\epsilon_{\alpha,\beta}(k) = \frac{1}{2}(\pm \Delta \epsilon_k + \gamma_k)$, with $\gamma_k = [(A_k + B_k - 4D_c)^2 - 4C_k^2]^{1/2}$ and the energy splitting $\Delta \epsilon_k^{\text{magnon}}$ between the two magnon modes is

$$\Delta \epsilon_k^{\text{magnon}} = \epsilon_\alpha(k) - \epsilon_\beta(k) = 4(J_7^b - J_7^a) \sin(k_x a) \sin(k_y a). \quad (3)$$

This constitutes an analytical demonstration of the splitting between the magnon bands (see Fig. 1b) occurring due to the direction-dependent exchange coupling J_7 . It is also clear from Eq. (3) that $\Delta \epsilon_k^{\text{magnon}}$ switches sign under C_{4z} rotation of the wave vector \vec{k} , leading to a d -wave splitting similar to the NRSS in the electronic

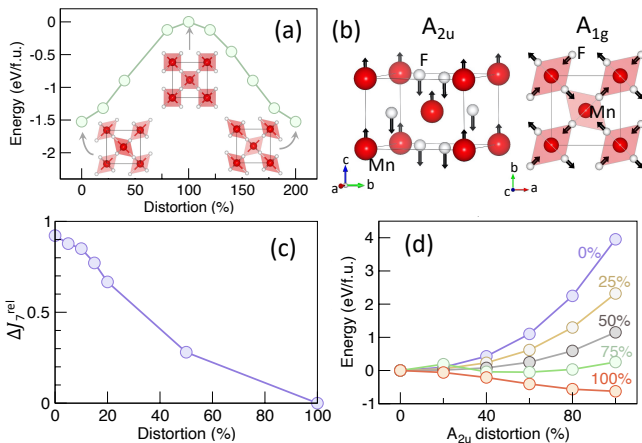


FIG. 2. The effect of structural distortion. (a) The variation in the total energy as a function of distortion amplitude. The 0%, 100%, and 200% distortions correspond to the actual crystal structure, the higher energy structure with zero spin splitting, and the opposite structural domain with opposite spin splitting. (b) Pictorial depiction of A_{2u} (left) and A_{1g} (right) phonon modes. The black arrows indicate the displacements of the Mn and F ions in the unit cell. (c) The dependence of ΔJ_7^{rel} on the amplitude of the combined control of the phonon modes A_{2u} and A_{1g} . (d) The total energy as a function of A_{2u} distortion for different amplitudes of A_{1g} distortions, showing that the structure with stronger A_{2u} distortion also energetically favors stronger A_{1g} distortion.

bands. We note that the calculated magnon band splitting, $\Delta\varepsilon_k^{\text{magnon}}$, is small in magnitude (~ 0.02 meV) for MnF_2 . A recent *unpolarized* inelastic neutron scattering experiment, with a resolution of approximately 0.1 meV [71], did not detect this splitting and concluded that it is absent, suggesting the need for techniques such as polarized neutrons or circularly polarized photons, which are sensitive to the handedness of magnons. Interestingly, our calculations show that at $\vec{k} \equiv (\pm \frac{\pi}{2a}, \pm \frac{\pi}{2a}, \pm \frac{\pi}{c})$, the splitting $\Delta\varepsilon_k^{\text{magnon}}$ is not only maximum but also the eigenvectors take the form $[1 \ 0]^T$ and $[0 \ 1]^T$, exhibiting *pure* left- and right-handedness. This indicates a stronger coupling of magnon bands to circularly polarized light or polarized neutrons at these momentum points.

Control of magnon splitting. Since the magnon splitting $\Delta\varepsilon_k^{\text{magnon}}$ originates from the inequivalent J_7 exchange couplings, $\Delta\varepsilon_k^{\text{magnon}}$ can be tuned by controlling the difference $\Delta J_7 = (J_7^b - J_7^a)$. Furthermore, since ΔJ_7 results from the inequivalent F environment around the Mn ions for the different exchange paths corresponding to J_7^a and J_7^b , we can control ΔJ_7 and hence the magnon splitting by manipulating the position of the F atoms.

With this idea, we construct a higher-energy structure with zero spin splitting, corresponding to the space group $P4_2/nm$, by linearly interpolating the two structural domains of MnF_2 (see the inset of Fig. 2a) with opposite spin splitting [49]. In this structure, the F atoms are shifted from the plane containing the Mn atoms such

that no F atoms are present between the seventh neighbor Mn atoms. We emphasize that our choice of the higher-energy structure with zero spin splitting is not unique. However, it is guided by the fact that the distortion linked to this reference $P4_2/nm$ structure can be represented in terms of the two stable Γ optical phonon modes corresponding to the A_{2u} and A_{1g} irreducible representations (IRs) of the ground state $P4_2/mnm$ structure. We identify these phonon modes by explicitly carrying out the phonon calculations for the ground state $P4_2/mnm$ structure using the finite difference method as implemented within the Phonopy [72] and then projecting the distorted $P4_2/nm$ structure on the Γ point phonon eigenvectors of the $P4_2/mnm$ structure [73, 74].

We note that the polar distortion A_{2u} is infrared active [54], describing the displacements of the Mn and F atoms in the opposite direction along the c axis (see Fig. 2b) such that it lowers the symmetry of the structure to $P4_2nm$. In contrast, the A_{1g} phonon mode is isosymmetric and Raman-active. The A_{1g} phonon mode describes the displacement of the F atoms on the ab plane, as depicted in Fig. 2b, which resembles the Q_{2z} Jahn-Teller distortion [75] of the MnF_6 octahedra. The computed frequencies of the A_{2u} and A_{1g} phonon modes are, respectively, 284 cm^{-1} (8.52 THz) and 325 cm^{-1} (9.74 THz).

We now show that magnon splitting indeed can be tuned by jointly controlling the two phonon mode distortions. For this, we construct several intermediate structures between the ground state structure $P4_2/mnm$ and the higher energy structure $P4_2/nm$ by varying the amplitudes of the atomic distortions as $\beta(Q_{A_{2u}} + Q_{A_{1g}})$. Here, $Q_{A_{2u}}$ and $Q_{A_{1g}}$ are the atomic distortions corresponding to the A_{2u} and A_{1g} phonon modes respectively [76], and β varies between 0 to 1 which correspond to 0% ($P4_2/mnm$) and 100% ($P4_2/nm$) of atomic distortions respectively. We then compute the variation of the exchange interactions across these intermediate structures. The resulting change ΔJ_7^{rel} in the seventh NN coupling, $\Delta J_7^{\text{rel}} = \left| \frac{\Delta J_7}{(J_7^a + J_7^b)} \right|$, is shown in Fig. 2c. As we see from the plot, ΔJ_7^{rel} gradually decreases with an increase in the distortion and eventually vanishes at the higher energy $P4_2/nm$ structure (See Fig. 2c), consistent with the equivalent J_7 exchange paths. Consequently, we can tune the magnon splitting $\Delta\varepsilon_k^{\text{magnon}}$ by controlling the amplitude of the structural distortion, as depicted in Fig. 1c. We note that with increasing distortion, J_2 and J_5 exchange couplings also gradually become inequivalent [65]. However, both being inter-sublattice coupling, the corresponding changes only affect the γ_k term in the magnon band dispersion and do not contribute to the splitting of the magnon bands $\Delta\varepsilon_k^{\text{magnon}}$ [65].

We emphasize that the magnon splitting control discussed here arises from changes in the nonmagnetic environment around the Mn ions, without changing the AFM order, as confirmed by our computed exchange couplings [65]. This “magnon splitting” is fundamentally different from the splitting reported in earlier works [45, 53, 77–79], which arises from magnon-phonon hybridization and

appears as an anti-crossing gap between magnon and phonon bands. In contrast, our work explores how structural distortions—driven by specific phonon modes—affect electronic and magnonic bands within the Born-Oppenheimer approximation, where these degrees of freedom respond instantaneously to changes in ionic positions.

To better rationalize the joint control of the A_{2u} and A_{1g} distortions, we perform a low-order Taylor expansion of the Born-Oppenheimer energy U around the ground-state $P4_2/mnm$ structure in terms of their respective amplitudes $Q_{A_{2u}}$ and $Q_{A_{1g}}$ [80–82]:

$$U \approx \alpha_1 Q_{A_{1g}}^2 + \alpha_2 Q_{A_{1g}}^4 + \beta_1 Q_{A_{2u}}^2 + \beta_2 Q_{A_{2u}}^4 + \lambda_1 Q_{A_{2u}}^2 Q_{A_{1g}} + \lambda_2 Q_{A_{2u}}^2 Q_{A_{1g}}^2 + O(Q^5). \quad (4)$$

By fitting DFT total energies of a set of structures with different combinations of $Q_{A_{2u}}$ and $Q_{A_{1g}}$ with Eq. (4), we extract the values of the coefficients: $\alpha_1 = 1.061$, $\alpha_2 = 0.346$, $\beta_1 = 2.944$, $\beta_2 = 0.907$, $\lambda_1 = -6.253$ and $\lambda_2 = 1.812$ eV/f.u. (see SM[65] for details). Using Eq. (4), we then compute the optimal values of $Q_{A_{1g}}$ for a given $Q_{A_{2u}}$, which interestingly vary as $Q_{A_{1g}} \approx Q_{A_{2u}}$, supporting the approximation we made previously.

In practice, infrared-active modes can be tuned using optical pulses, as shown in CoF₂ [52], or via an external electric field \mathcal{E}_z . To estimate the required field strength, we have added a term $-\Omega \mathcal{E}_z P_z$ to Eq. (4), with $P_z \propto Q_{A_{2u}}$ and Ω as the unit cell volume (see SM [65]). We find that \mathcal{E}_z of 6.5, 11.5, and 15 MV/cm induce 5%, 10%, and 15% of $Q_{A_{2u}}$ distortions, modifying the NRSS by 4%, 10%, and 18%, respectively. While these fields are large, they are potentially achievable [83–85]. This serves as a proof of concept, and the effect could be enhanced with a softer A_{2u} mode, possibly via alternative compounds [86] or strain engineering [65].

Connection to spin splitting in the electronic bands—To investigate the impact of joint control of A_{2u} and A_{1g} structural distortions on the electronic bands, we further analyze the corresponding electronic bands for intermediate distortions. The results are shown in Fig. 1d. As evident from the figure, the spin splitting between electronic bands decreases with increasing distortion and, eventually, vanishes for the higher-energy $P4_2/nm$ structure, similar to what we observe with the magnon bands. This indicates a correlation between the splitting in the electronic and magnonic bands.

To explore the origin of the connection between electronic and magnonic bands, we compute the band-decomposed magnetization density for the top pair of valence bands for structures with 0%, 80%, and 100% distortions. Here, 0% corresponds to the ground-state structure, while 100% refers to the $P4_2/nm$ structure with zero spin splitting. As seen in Figs. 3 a-c, the anisotropy in the magnetization density decreases with increasing distortion. For 0% distortion, the magnetization density around the Mn ions is highly anisotropic, taking on an elliptical shape, with the long axis aligned along the Mn-Mn bond corresponding to the seventh neighbor, with

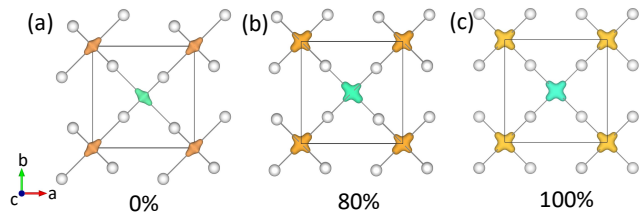


FIG. 3. The computed magnetization densities for three different distortion amplitudes (a) 0%, (b) 80%, and (c) 100%. The isosurface value is set to 0.1 for all the plots. Different colors of the magnetization density denote the opposite spin polarization around the corner and center Mn ions. The white balls represent the F atoms.

two F atoms between them. This anisotropic magnetization is linked to the direction-dependent J_7 exchange coupling as the larger magnetization density implies a stronger interaction along that particular Mn-Mn bond.

Interestingly, the anisotropic magnetization density, described by the magnetic octupole, has previously been shown to play a key role in the spin splitting of electronic bands [49]. The computed magnitude of the ferriocally ordered atomic site magnetic octupole component $\mathcal{O}_{32-} = -2.5 \times 10^{-3} \mu_B$ per Mn atom. As distortion increases, the F atoms move away from the Mn-Mn bond, and the magnetization density shifts to form two ellipsoids along the Mn-Mn bonds associated with J_7 , thus reducing ΔJ_7^{rel} . At 100% distortion, the anisotropy in the magnetization density is minimized, and our multipole calculations [65, 87–89] show the absence of ferrioc magnetic octupoles with $\mathcal{O}_{32-} = 0$. This demonstrates a transition from an “altermagnetic” state with ferromagnetoctupole to a conventional antiferromagnetic state with no ferrioc magnetic octupole and NRSS. Correspondingly, ΔJ_7^{rel} also vanishes, resulting in an absence of splitting between the magnon bands, revealing the origin of the connection between splitting in the electronic and magnonic bands.

The structural manipulation of electronic and magnonic splitting demonstrated in our study extends beyond MnF₂ and related difluorides. Recent predictions [55–57, 86] of NRSS tuning via electric field or strain further reinforce our findings. The proposed concept is general and also applies to other SSAFMs, including those exhibiting g -wave spin splitting with anisotropic magnetization density, characterized by magnetic triakontadipoles [90, 91] rather than magnetic octupoles. While the specific phonon modes may vary across different materials, it remains feasible to control the positioning of nonmagnetic ligand atoms by carefully analyzing the relevant phonon distortion modes, thus enabling the regulation of splitting in both magnon and electronic bands.

To summarize, our work uncovers the intricate correlation between phonons, electrons, and magnons in SSAFMs, by explicitly demonstrating the control of the

dispersion relation for the last two by tuning the former. The proposed phonon-assisted manipulation of the magnon and electronic splitting may be probed using time-resolved magneto-optical Kerr measurements and time-resolved resonant inelastic scattering measurements. Interestingly, a recent study on CoF_2 demonstrates the coupling between magnons and infrared-active polar phonons through dynamic modulation of magnetic exchange interactions using far-infrared and dielectric spectroscopy techniques [54] — going beyond the conventional avoided crossing between phonons and magnons. These results offer a promising experimental approach to test and validate the control mechanism we propose for MnF_2 . We hope that our work will open up a new paradigm for ultra-fast manipulation of SSAFMs, motivating future research along these directions.

ACKNOWLEDGEMENTS

We thank Abhishek Nag, Urs Staub, and Nicola A. Spaldin for stimulating discussions. SBa acknowledges

use of the CECI supercomputer facilities funded by the F.R.S-FNRS (Grant No. 2.5020.1) and of the Tier-1 supercomputer of the Fédération Wallonie-Bruxelles funded by the Walloon Region (Grant No. 1117545). AR acknowledges the financial support provided by CSIR-HRDG, India, in the form of a Senior Research Fellowship (SRF). SP acknowledges financial support from SERB, DST, Govt. of India (Grant No. MTR/2022/000386) and partially by Grant No. CRG/2021/003024. SBh thanks National Supercomputing Mission for providing computing resources of ‘PARAM Porul’ at NIT Trichy, implemented by C-DAC and supported by the Ministry of Electronics and Information Technology (MeitY) and Department of Science and Technology, Government of India and acknowledges funding support from the Industrial Research and Consultancy Centre (IRCC) Seed Grant (RD/0523-IRCCSH0-018) and the INSPIRE research grant (project code RD/0124-DST0030-002).

-
- [1] S. Hayami, Y. Yanagi, and H. Kusunose, Momentum-dependent spin splitting by collinear antiferromagnetic ordering, *J. Phys. Soc. Jpn.* **88**, 123702 (2019).
- [2] L.-D. Yuan, Z. Wang, J.-W. Luo, E. I. Rashba, and A. Zunger, Giant momentum-dependent spin splitting in centrosymmetric low- z antiferromagnets, *Phys. Rev. B* **102**, 014422 (2020).
- [3] L.-D. Yuan, Z. Wang, J.-W. Luo, and A. Zunger, Prediction of low- z collinear and noncollinear antiferromagnetic compounds having momentum-dependent spin splitting even without spin-orbit coupling, *Phys. Rev. Materials* **5**, 014409 (2021).
- [4] L. Šmejkal, J. Sinova, and T. Jungwirth, Beyond conventional ferromagnetism and antiferromagnetism: A phase with nonrelativistic spin and crystal rotation symmetry, *Phys. Rev. X* **12**, 031042 (2022).
- [5] L.-D. Yuan and A. Zunger, Degeneracy removal of spin bands in collinear antiferromagnets with non-interconvertible spin-structure motif pair, *Advanced Materials* **35**, 2211966 (2023).
- [6] Y. Guo, H. Liu, O. Janson, I. C. Fulga, J. van den Brink, and J. I. Facio, Spin-split collinear antiferromagnets: A large-scale ab-initio study, *Mater. Today Phys.* **32**, 100991 (2023).
- [7] S. Zeng and Y.-J. Zhao, Description of two-dimensional altermagnetism: Categorization using spin group theory, *Phys. Rev. B* **110**, 054406 (2024).
- [8] S. Lee, S. Lee, S. Jung, J. Jung, D. Kim, Y. Lee, B. Seok, J. Kim, B. G. Park, L. Šmejkal, C.-J. Kang, and C. Kim, Broken Kramers degeneracy in altermagnetic MnTe, *Phys. Rev. Lett.* **132**, 036702 (2024).
- [9] J. Krempaský, L. Šmejkal, S. W. D’Souza, M. Hajaoui, G. Springholz, K. Uhlířová, F. Alarab, P. C. Constantinou, V. Strocov, D. Usanov, W. R. Pudelko, R. González-Hernández, A. Birk Hellenes, Z. Jansa, H. Reichlová, Z. Šobáň, R. D. Gonzalez Betancourt, P. Wadley, J. Sinova, D. Kriegner, J. Minár, J. H. Dil, and T. Jungwirth, Altermagnetic lifting of Kramers spin degeneracy, *Nature* **626**, 517 (2024).
- [10] S. Reimers, L. Odenbreit, L. Šmejkal, V. N. Strocov, P. Constantinou, A. B. Hellenes, R. Jaeschke Ubierno, W. H. Campos, V. K. Bharadwaj, A. Chakraborty, T. Denneulin, W. Shi, R. E. Dunin-Borkowski, S. Das, M. Kläui, J. Sinova, and M. Jourdan, Direct observation of altermagnetic band splitting in CrSb thin films, *Nat. Commun.* **15**, 2116 (2024).
- [11] T. Aoyama and K. Ohgushi, Piezomagnetic properties in altermagnetic MnTe, *Phys. Rev. Mater.* **8**, L041402 (2024).
- [12] Z. Lin, D. Chen, W. Lu, X. Liang, S. Feng, K. Yamagami, J. Osiecki, M. Leandersson, B. Thiagarajan, J. Liu, C. Felser, and J. Ma, Observation of giant spin splitting and d-wave spin texture in room temperature altermagnet RuO_2 (2024), arXiv:2402.04995 [cond-mat.mtrl-sci].
- [13] K.-H. Ahn, A. Hariki, K.-W. Lee, and J. Kuneš, Antiferromagnetism in RuO_2 as d -wave Pomeranchuk instability, *Phys. Rev. B* **99**, 184432 (2019).
- [14] L. Šmejkal, R. González-Hernández, T. Jungwirth, and J. Sinova, Crystal time-reversal symmetry breaking and spontaneous Hall effect in collinear antiferromagnets, *Sci. Adv.* **6**, eaaz8809 (2020), <https://www.science.org/doi/pdf/10.1126/sciadv.aaz8809>.
- [15] L. Šmejkal, J. Sinova, and T. Jungwirth, Emerging research landscape of altermagnetism, *Phys. Rev. X* **12**, 040501 (2022).
- [16] P. A. McClarty and J. G. Rau, Landau theory of altermagnetism, *Phys. Rev. Lett.* **132**, 176702 (2024).
- [17] L. Bai, W. Feng, S. Liu, L. Šmejkal, Y. Mokrousov, and Y. Yao, Altermagnetism: Exploring new frontiers in magnetism and spintronics (2024), arXiv:2406.02123 [cond-

- mat.mtrl-sci].
- [18] M. Naka, S. Hayami, H. Kusunose, Y. Yanagi, Y. Motome, and H. Seo, Spin current generation in organic antiferromagnets, *Nat. Commun.* **10**, 4305 (2019).
- [19] R. González-Hernández, L. Šmejkal, K. Výborný, Y. Yahagi, J. Sinova, T. Jungwirth, and J. Železný, Efficient electrical spin splitter based on nonrelativistic collinear antiferromagnetism, *Phys. Rev. Lett.* **126**, 127701 (2021).
- [20] D.-F. Shao, S.-H. Zhang, M. Li, C.-B. Eom, and E. Y. Tsybal, Spin-neutral currents for spintronics, *Nat. Commun.* **12**, 7061 (2021).
- [21] A. Bose, N. J. Schreiber, R. Jain, D.-F. Shao, H. P. Nair, J. Sun, X. S. Zhang, D. A. Muller, E. Y. Tsybal, D. G. Schlom, and D. C. Ralph, Tilted spin current generated by the collinear antiferromagnet ruthenium dioxide, *Nat. Electron.* **5**, 267 (2022).
- [22] M. Hu, O. Janson, C. Felser, P. McClarty, J. van den Brink, and M. G. Vergniory, Spin Hall and edelstein effects in novel chiral noncollinear altermagnets (2024), arXiv:2410.17993 [cond-mat.mtrl-sci].
- [23] H. Bai, L. Han, X. Y. Feng, Y. J. Zhou, R. X. Su, Q. Wang, L. Y. Liao, W. X. Zhu, X. Z. Chen, F. Pan, X. L. Fan, and C. Song, Observation of spin splitting torque in a collinear antiferromagnet RuO₂, *Phys. Rev. Lett.* **128**, 197202 (2022).
- [24] S. Karube, T. Tanaka, D. Sugawara, N. Kadoguchi, M. Kohda, and J. Nitta, Observation of spin-splitter torque in collinear antiferromagnetic RuO₂, *Phys. Rev. Lett.* **129**, 137201 (2022).
- [25] L. Šmejkal, A. B. Hellenes, R. González-Hernández, J. Sinova, and T. Jungwirth, Giant and tunneling magnetoresistance in unconventional collinear antiferromagnets with nonrelativistic spin-momentum coupling, *Phys. Rev. X* **12**, 011028 (2022).
- [26] L. Šmejkal, A. H. MacDonald, J. Sinova, S. Nakatsuji, and T. Jungwirth, Anomalous Hall antiferromagnets, *Nature Reviews Materials* **7**, 482 (2022).
- [27] H. Reichlová, R. L. Seeger, R. González-Hernández, I. Kounta, R. Schlitz, D. Kriegner, P. Ritzinger, M. Lammel, M. Leiviskä, V. Petříček, P. Doležal, E. Schmoranzarová, A. Bad'ura, A. Thomas, V. Baltz, L. Michez, J. Sinova, S. T. B. Goennenwein, T. Jungwirth, and L. Šmejkal, Macroscopic time reversal symmetry breaking by staggered spin-momentum interaction, arXiv 2012.15651 (2020).
- [28] Z. Feng, X. Zhou, L. Šmejkal, L. Wu, Z. Zhu, H. Guo, R. González-Hernández, X. Wang, H. Yan, P. Qin, X. Zhang, H. Wu, H. Chen, Z. Meng, L. Liu, Z. Xia, J. Sinova, T. Jungwirth, and Z. Liu, An anomalous Hall effect in altermagnetic ruthenium dioxide, *Nat. Electron.* **5**, 735 (2022).
- [29] R. D. Gonzalez Betancourt, J. Zubáč, R. Gonzalez-Hernandez, K. Geishendorf, Z. Šobáň, G. Springholz, K. Olejník, L. Šmejkal, J. Sinova, T. Jungwirth, S. T. B. Goennenwein, A. Thomas, H. Reichlová, J. Železný, and D. Kriegner, Spontaneous anomalous Hall effect arising from an unconventional compensated magnetic phase in a semiconductor, *Phys. Rev. Lett.* **130**, 036702 (2023).
- [30] L. Šmejkal, A. H. MacDonald, J. Sinova, S. Nakatsuji, and T. Jungwirth, Anomalous Hall antiferromagnets, *Nat. Rev. Mater.* **7**, 482 (2022).
- [31] S.-W. Cheong and F.-T. Huang, Altermagnetism with non-collinear spins, *npj Quantum Materials* **9**, 13 (2024).
- [32] T. Sato, S. Haddad, I. C. Fulga, F. F. Assaad, and J. van den Brink, Altermagnetic anomalous Hall effect emerging from electronic correlations, *Phys. Rev. Lett.* **133**, 086503 (2024).
- [33] I. I. Mazin, Notes on altermagnetism and superconductivity, arXiv 2203.05000 (2022).
- [34] D. Zhu, Z.-Y. Zhuang, Z. Wu, and Z. Yan, Topological superconductivity in two-dimensional altermagnetic metals, *Phys. Rev. B* **108**, 184505 (2023).
- [35] S. Banerjee and M. S. Scheurer, Altermagnetic superconducting diode effect, *Phys. Rev. B* **110**, 024503 (2024).
- [36] D. Chakraborty and A. M. Black-Schaffer, Zero-field finite-momentum and field-induced superconductivity in altermagnets, *Phys. Rev. B* **110**, L060508 (2024).
- [37] S.-B. Zhang, L.-H. Hu, and T. Neupert, Finite-momentum cooper pairing in proximitized altermagnets, *Nat. Commun.* **15**, 1801 (2024).
- [38] S. H. Lee, Y. Qian, and B.-J. Yang, Fermi surface spin texture and topological superconductivity in spin-orbit free noncollinear antiferromagnets, *Phys. Rev. Lett.* **132**, 196602 (2024).
- [39] X. Zhou, W. Feng, R.-W. Zhang, L. Šmejkal, J. Sinova, Y. Mokrousov, and Y. Yao, Crystal thermal transport in altermagnetic ruo₂, *Phys. Rev. Lett.* **132**, 056701 (2024).
- [40] K. V. Yershov, V. P. Kravchuk, M. Daghofer, and J. van den Brink, Fluctuation-induced piezomagnetism in local moment altermagnets, *Phys. Rev. B* **110**, 144421 (2024).
- [41] L. Šmejkal, A. Marmodoro, K.-H. Ahn, R. González-Hernández, I. Turek, S. Mankovsky, H. Ebert, S. W. D'Souza, O. c. v. Šipr, J. Sinova, and T. c. v. Jungwirth, Chiral magnons in altermagnetic RuO₂, *Phys. Rev. Lett.* **131**, 256703 (2023).
- [42] P. A. McClarty, A. Gukasov, and J. G. Rau, Observing altermagnetism using polarized neutrons (2024), arXiv:2410.10771 [cond-mat.str-el].
- [43] Z. Liu, M. Ozeki, S. Asai, S. Itoh, and T. Masuda, Chiral split magnon in altermagnetic MnTe, *Phys. Rev. Lett.* **133**, 156702 (2024).
- [44] We will stick to handedness in the rest of the article.
- [45] Q. Cui, B. Zeng, P. Cui, T. Yu, and H. Yang, Efficient spin seebeck and spin nernst effects of magnons in altermagnets, *Phys. Rev. B* **108**, L180401 (2023).
- [46] W. de Haas, B. Schultz, and J. Koolhaas, Further measurements of the magnetic properties of some salts of the iron group at low temperatures, *Physica* **7**, 57 (1940).
- [47] M. S. Seehra and R. E. Helmick, Anomalous changes in the dielectric constants of MnF₂ near its néel temperature, *J. Appl. Phys.* **55**, 2330 (1984).
- [48] Z. Yamani, Z. Tun, and D. H. Ryan, Neutron scattering study of the classical antiferromagnet MnF₂: a perfect hands-on neutron scattering teaching course, *Can. J. Phys.* **88**, 771 (2010).
- [49] S. Bhowal and N. A. Spaldin, Ferroically ordered magnetic octupoles in *d*-wave altermagnets, *Phys. Rev. X* **14**, 011019 (2024).
- [50] M. Costa and P. Brown, Magnetisation density in MnF₂, *Physica B: Condensed Matter* **156-157**, 329 (1989).
- [51] E. A. Mashkovich, K. A. Grishunin, R. M. Dubrovin, A. K. Zvezdin, R. V. Pisarev, and A. V. Kimel, Terahertz light-driven coupling of antiferromagnetic spins to lattice, *Science* **374**, 1608 (2021).
- [52] A. S. Disa, M. Fechner, T. F. Nova, B. Liu, M. Först, D. Prabhakaran, P. G. Radaelli, and A. Cavalleri, Po-

- larizing an antiferromagnet by optical engineering of the crystal field, *Nat. Phys.* **16**, 937 (2020).
- [53] T. W. J. Metzger, K. A. Grishunin, C. Reinhoﬀer, R. M. Dubrovin, A. Arshad, I. Ilyakov, T. V. A. G. de Oliveira, A. Ponomaryov, J.-C. Deinert, S. Kovalev, R. V. Pisarev, M. I. Katsnelson, B. A. Ivanov, P. H. M. van Loosdrecht, A. V. Kimel, and E. A. Mashkovich, Magnon-phonon fermi resonance in antiferromagnetic CoF_2 , *Nat. Commun.* **15**, 5472 (2024).
- [54] R. M. Dubrovin, A. Tellez-Mora, A. C. Garcia-Castro, N. V. Siverin, N. N. Novikova, K. N. Boldyrev, E. A. Mashkovich, A. H. Romero, and R. V. Pisarev, Polar phonons and magnetic excitations in the antiferromagnet CoF_2 , *Phys. Rev. B* **109**, 224312 (2024).
- [55] X. Duan, J. Zhang, Z. Zhu, Y. Liu, Z. Zhang, I. Žutić, and T. Zhou, Antiferroelectric altermagnets: Antiferroelectricity alters magnets, *Phys. Rev. Lett.* **134**, 106801 (2025).
- [56] M. Gu, Y. Liu, H. Zhu, K. Yananose, X. Chen, Y. Hu, A. Stroppa, and Q. Liu, Ferroelectric switchable altermagnetism, *Phys. Rev. Lett.* **134**, 106802 (2025).
- [57] L. Šmejkal, Altermagnetic multiferroics and altermagnetoelectric effect (2024), arXiv:2411.19928 [cond-mat.mtrl-sci].
- [58] A. Kirilyuk, A. V. Kimel, and T. Rasing, Ultrafast optical manipulation of magnetic order, *Rev. Mod. Phys.* **82**, 2731 (2010).
- [59] P. E. Blöchl, Projector augmented-wave method, *Phys. Rev. B* **50**, 17953 (1994).
- [60] G. Kresse and D. Joubert, From ultrasoft pseudopotentials to the projector augmented-wave method, *Phys. Rev. B* **59**, 1758 (1999).
- [61] G. Kresse and J. Hafner, Ab initio molecular dynamics for liquid metals, *Phys. Rev. B* **47**, 558 (1993).
- [62] G. Kresse and J. Furthmüller, Efficient iterative schemes for ab initio total-energy calculations using a plane-wave basis set, *Phys. Rev. B* **54**, 11169 (1996).
- [63] H. J. Xiang, E. J. Kan, S.-H. Wei, M.-H. Whangbo, and X. G. Gong, Predicting the spin-lattice order of frustrated systems from first principles, *Phys. Rev. B* **84**, 224429 (2011).
- [64] D. Šabani, C. Bacaksiz, and M. V. Milošević, Ab initio methodology for magnetic exchange parameters: Generic four-state energy mapping onto a heisenberg spin hamiltonian, *Phys. Rev. B* **102**, 014457 (2020).
- [65] Supplemental materials for the computational details of the DFT and the magnon calculations, and the additional results for the exchange coupling calculations.
- [66] Although Ref. [41] considers an antiferromagnetic ground state, the ground state magnetism of RuO_2 remains debatable [67–69].
- [67] A. Smolyanyuk, I. I. Mazin, L. Garcia-Gassull, and R. Valentí, Fragility of the magnetic order in the prototypical altermagnet RuO_2 , *Phys. Rev. B* **109**, 134424 (2024).
- [68] M. Hiraishi, H. Okabe, A. Koda, R. Kadono, T. Muroi, D. Hirai, and Z. Hiroi, Nonmagnetic ground state in RuO_2 revealed by muon spin rotation, *Phys. Rev. Lett.* **132**, 166702 (2024).
- [69] P. Keßler, L. Garcia-Gassull, A. Suter, T. Prokscha, Z. Salman, D. Khalyavin, P. Manuel, F. Orlandi, I. I. Mazin, R. Valentí, and S. Moser, Absence of magnetic order in RuO_2 : insights from μsr spectroscopy and neutron diffraction, *npj Spintronics* **2**, 50 (2024).
- [70] T. Holstein and H. Primakoff, Field dependence of the intrinsic domain magnetization of a ferromagnet, *Phys. Rev.* **58**, 1098 (1940).
- [71] V. C. Morano, Z. Maesen, S. E. Nikitin, J. Lass, D. G. Mazzone, and O. Zaharko, Absence of altermagnetic magnon band splitting in MnF_2 (2024), arXiv:2412.03545 [cond-mat.str-el].
- [72] A. Togo and I. Tanaka, First principles phonon calculations in materials science, *Scripta Materialia* **108**, 1 (2015).
- [73] H. T. Stokes, D. M. Hatch, and B. J. Campbell, ISODISTORT, ISOTROPY software suite, <https://iso.byu.edu> ().
- [74] B. J. Campbell, H. T. Stokes, D. E. Tanner, and D. M. Hatch, *ISODISPLACE*: a web-based tool for exploring structural distortions, *Journal of Applied Crystallography* **39**, 607 (2006).
- [75] S. Bandyopadhyay and P. Ghosez, Structurally triggered orbital and charge orderings in TlMnO_3 and related compounds (2024), arXiv:2407.21406 [cond-mat.str-el].
- [76] $Q_{A_{2u}}$ and $Q_{A_{1g}}$ are normalized to their amplitudes at $P4_2/nmm$ structure.
- [77] T. Hioki, Y. Hashimoto, and E. Saitoh, Coherent oscillation between phonons and magnons, *Communications Physics* **5**, 115 (2022).
- [78] S. Liu, A. Granados del Águila, D. Bhowmick, C. K. Gan, T. Thu Ha Do, M. A. Prosnikov, D. Sedmidubský, Z. Sofer, P. C. M. Christianen, P. Sengupta, and Q. Xiong, Direct observation of magnon-phonon strong coupling in two-dimensional antiferromagnet at high magnetic fields, *Phys. Rev. Lett.* **127**, 097401 (2021).
- [79] T. T. Mai, K. F. Garrity, A. McCreary, J. Argo, J. R. Simpson, V. Doan-Nguyen, R. V. Aguilar, and A. R. H. Walker, Magnon-phonon hybridization in 2d antiferromagnet MnPS_3 , *Science Advances* **7**, eabj3106 (2021).
- [80] The symmetry allowed terms in the free energy are obtained using the INVARIANTS software [81, 82].
- [81] H. T. Stokes, D. M. Hatch, and B. J. Campbell, INVARIANTS, ISOTROPY Software Suite ().
- [82] D. M. Hatch and H. T. Stokes, *INVARIANTS*: program for obtaining a list of invariant polynomials of the order-parameter components associated with irreducible representations of a space group, *Journal of Applied Crystallography* **36**, 951 (2003).
- [83] K. D. Kim, Y. B. Lee, S. H. Lee, I. S. Lee, S. K. Ryoo, S. Byun, J. H. Lee, H. Kim, H. W. Park, and C. S. Hwang, Evolution of the ferroelectric properties of alscn film by electrical cycling with an inhomogeneous field distribution, *Advanced Electronic Materials* **9**, 2201142 (2023).
- [84] J. Varignon, N. C. Bristowe, and P. Ghosez, Electric field control of jahn-teller distortions in bulk perovskites, *Phys. Rev. Lett.* **116**, 057602 (2016).
- [85] Y. Yang, J. Íñiguez, A.-J. Mao, and L. Bellaiche, Prediction of a novel magnetoelectric switching mechanism in multiferroics, *Phys. Rev. Lett.* **112**, 057202 (2014).
- [86] S. Bandyopadhyay, S. Picozzi, and S. Bhowal, Designing non-relativistic spin splitting in oxide perovskites (2025), arXiv:2503.17001 [cond-mat.mtrl-sci].
- [87] F. Cricchio, *Multipoles in Correlated Electron Materials*, Ph.D. thesis, Uppsala University (2010).
- [88] O. Grånäs, *Theoretical Studies of Magnetism and Electron Correlation in Solids*, Ph.D. thesis, Uppsala University (2012).

- [89] N. A. Spaldin, M. Fechner, E. Bousquet, A. Balatsky, and L. Nordström, Monopole-based formalism for the diagonal magnetoelectric response, *Phys. Rev. B* **88**, 094429 (2013).
- [90] X. H. Verbeek, D. Voderholzer, S. Schären, Y. Gachnang, N. A. Spaldin, and S. Bhowal, Nonrelativistic ferromagnetotriakontadipolar order and spin splitting in hematite, *Phys. Rev. Res.* **6**, 043157 (2024).
- [91] R. Hoyer, P. P. Stavropoulos, A. Razpopov, R. Valentí, L. Šmejkal, and A. Mook, Altermagnetic splitting of magnons in hematite (α - Fe_2O_3) (2025), arXiv:2503.11623 [cond-mat.str-el].
- [92] R. D. King-Smith and D. Vanderbilt, Theory of polarization of crystalline solids, *Phys. Rev. B* **47**, 1651 (1993).
- [93] R. Resta, Macroscopic electric polarization as a geometric quantum phase, *Europhysics Letters* **22**, 133 (1993).
- [94] R. Resta, Macroscopic polarization in crystalline dielectrics: the geometric phase approach, *Rev. Mod. Phys.* **66**, 899 (1994).

Supplemental Materials for Rational Control of Magnonic and Electronic Band Splittings

I. COMPUTATIONAL DETAILS

The electronic structure of MnF_2 , as presented in the manuscript, is computed using the plane-wave based projector augmented wave (PAW) [59, 60] method as implemented in the Vienna ab initio simulation package (VASP) [61, 62]. All the calculations are performed using the LDA+ U formalism with $U_{\text{eff}} = 5$ eV at the Mn site [2]. To achieve self-consistency, we use an energy cut-off of 550 eV and a $10 \times 10 \times 14$ k-point sampling of the Brillouin zone. The PAW potentials Mn-pv ($[\text{Mg}]3p^63d^54s^2$) and F ($[\text{He}]2s^22p^5$) are employed in the calculations. All the calculations are performed using the relaxed structure of MnF_2 . The atomic relaxations are carried out until the Hellman-Feynman forces on each atom become less than 0.005 eV/Å. The atomic-site multipoles at the Mn ions are calculated from the decomposition of the density matrix $\rho_{lm,l'm'}$, computed within the framework of density functional theory (DFT), into the tensor moments [87–89], of which the parity even tensor moments have contributions from the $l = l'$ terms.

The exchange coupling J_i between two Mn atoms at different distances is computed using the methodology described in Refs. [63, 64]. We have calculated J_i up to the seventh nearest neighbor (NN). To calculate the exchange coupling between two particular Mn atoms, we compute the total energy within LDA+ U for four different collinear magnetic configurations while other Mn atoms are fixed to a ferromagnetic (FM) alignment. While calculating J , we used an adequate size of supercells to isolate the chosen two Mn atoms (between which

the exchange coupling is to be calculated) and avoid undesired contributions from other neighbors. Accordingly, $[1 \times 1 \times 4]$, $[1 \times 1 \times 4]$, $[2 \times 2 \times 2]$, $[4 \times 2 \times 2]$, $[3 \times 3 \times 3]$, $[2 \times 2 \times 4]$, $[2 \times 2 \times 5]$, $[4 \times 4 \times 2]$ supercells are used to calculate J_i s from first to seventh neighbours respectively. As the values of J are very small, we paid special attention to reduce numerical error while calculating them. We set a tolerance of 10^{-8} eV for the energy convergence during the electronic self-consistent calculations, which provided us the desired accuracy. We also calculate the easy-axis anisotropy energy $D_c \sum_i (S_i^z)^2$ by computing the energy difference between AFM configurations with spin polarization along \hat{x} and \hat{z} in the presence of spin-orbit coupling. The computed value of D_c is 1.2 μeV .

TABLE I. Frequencies of the optical phonon modes at the Γ point

index	frequency (cm^{-1})	index	frequency (cm^{-1})
4	63	12	247
5	119	13	284
6	157	14	318
7	157	15	325
8	220	16	348
9	234	17	348
10	234	18	453
11	247		

The phonon band structure for the ground state $P4_2/mnm$ structure of MnF_2 is computed using the finite difference method as implemented within the PHONOPY software [72]. The $P4_2/mnm$ structure of MnF_2 has six atoms in the unit cell. For the phonon band structure calculation, we considered a $2 \times 2 \times 2$ supercell, keeping the ground state antiferromagnetic (AFM) spin alignment. No unstable phonon mode is found in our calculation, confirming the dynamic stability of the $P4_2/mnm$ structure. Frequencies of the 15 optical phonon modes at the Γ point are given in Table I.

To obtain the high-energy $P4_2/nmm$ structure with zero spin and magnon splitting, we first construct the other structural domain with the same space group symmetry $P4_2/nmm$ but of opposite spin splitting [49]. The structure $P4_2/nmm$ is then obtained by linearly interpolating the two structures with opposite spin splitting. Distortions of the $P4_2/nmm$ structure can be described by the Γ point phonon modes of the ground state $P4_2/mnm$ structure, which are identified using the following two steps. First, we calculate the atomic distortions of $P4_2/nmm$ relative to the $P4_2/mnm$ structure. This provides distortions in all three Cartesian directions. Next, these distortions are mapped to the phonon eigenvectors at the Γ point as given below,

$$u_x \hat{x} + u_y \hat{y} + u_z \hat{z} = \sum_i c_i \vec{\Gamma}_i \quad (5)$$

Here, u_j with $j = x, y, z$ are the atomic distortions, and

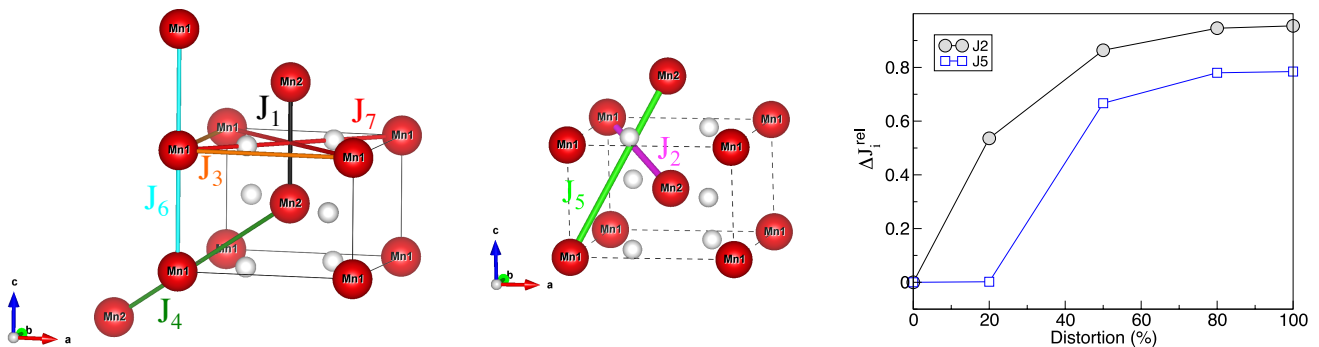


FIG. 4. Magnetic exchange interaction paths J_i , with $i=1$ to 7, between the Mn atoms. The left and middle panels show the inter-sublattice and intra-sublattice Mn–Mn interaction paths, respectively. The right panel shows the variation of ΔJ_i^{rel} for $i = 2$ and 5 as a function of amplitude of distortion.

c_i s are the amplitude of the Γ point phonon i ($i = 1, \dots, 24$) mode with eigenvector $\vec{\Gamma}_i$. We find that the reference structure, $P4_2/nmm$, with zero spin splitting contains distortion of the two stable Γ -phonon modes lying at 284 cm^{-1} (8.52 THz) and 325 cm^{-1} (9.74 THz) respectively with A_{2u} and A_{1g} irreducible representations (IRs), indexed as optical phonon modes 13 and 15 in Table I. We normalize $c_{A_{2u}}$ and $c_{A_{1g}}$ to 1, which correspond to atomic distortions of 0.83\AA and 0.38\AA respectively as calculated using ISODISTORT[73, 74].

II. ADDITIONAL RESULTS OF THE EXCHANGE COUPLINGS

TABLE II. Mn–Mn bond distances for the magnetic exchange interactions J_i .

J_i	Mn–Mn distance (\AA)
J_1	3.35
J_2	3.89
J_3	4.97
J_4	5.99
J_5	6.13
J_6	6.70
J_7	7.03

The exchange couplings J_i up to the seventh NNs for the ground state $P4_2/nmm$ structure are indicated in Fig. 4 (a-b) and their computed values are shown in Fig. 5. The corresponding distances are also listed in Table II. ΔJ_7 vanishes for $P4_2/nmm$ structure, explaining the suppression of the magnon band splitting. We note that the J_2 and J_5 exchange couplings, in contrast, become inequivalent for the $P4_2/nmm$ structure. We further compute $\Delta J_i^{\text{rel}} = \left| \frac{J_i^a - J_i^b}{J_i^a + J_i^b} \right|$ with $i = 2, 5$ for intermediate structures with different amplitudes of distortion, and the results are shown in Fig. 4c. ΔJ_i^{rel} with $i = 2, 5$,

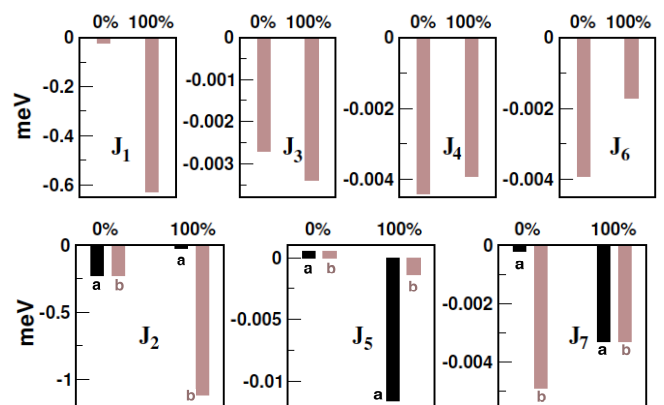


FIG. 5. Comparison of magnetic exchange interactions J_i between the $P4_2/nmm$ (0%) and $P4_2/nmm$ (100%) structures.

however, does not contribute to the splitting between magnon bands.

III. DETAILS OF THE MAGNON SPECTRUM

In the main text, we analytically demonstrated that the direction-dependent J_7 exchange coupling is responsible for the splitting between the magnon modes in MnF_2 , consistent with previous numerical results for the isostructural RuO_2 [41]. Here we present more details in obtaining the analytical solution for the magnon dispersion, including the explicit forms of A_k , B_k , and C_k from Eq. (1) in the main text. We use the Holstein-Primakoff transformation [70] to map the spin operator, S , to bosonic creation (annihilation) operators b_i^\dagger (b_i) and a_i^\dagger (a_i) on the two sublattices. Here, the creation of the ‘ a ’ (‘ b ’) boson at lattice site i corresponds to reducing (increasing) the magnitude of the spin moment from S to $S - 1$ ($-S + 1$) under the assumption $S \gg 1$, relevant to Mn^{2+} : $S = 5/2$ in MnF_2 . Using the Fourier

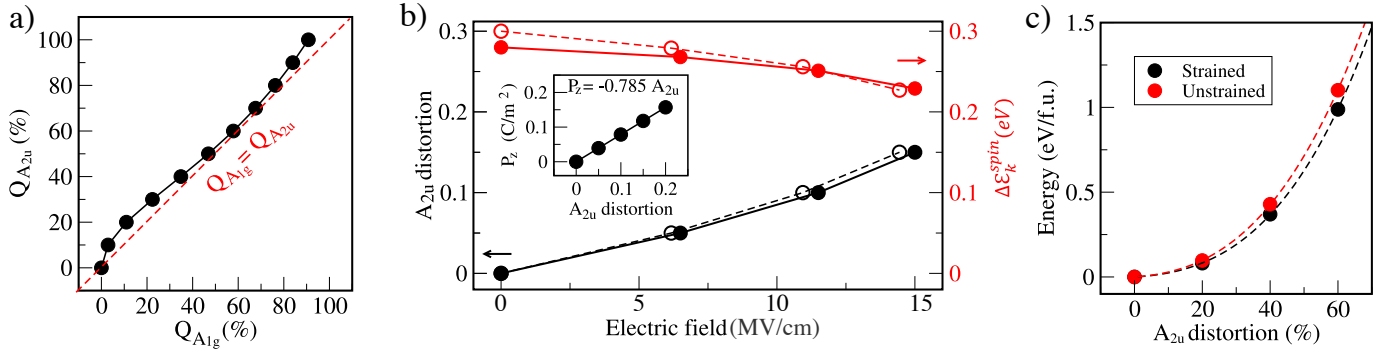


FIG. 6. (a) Variation of $Q_{A_{2u}}$ as a function of $Q_{A_{1g}}$. Black line and dots represent the calculated optimal values of $Q_{A_{2u}}$ for fixed values of $Q_{A_{1g}}$. Red dashed line indicates $Q_{A_{1g}} = Q_{A_{2u}}$. (b) Variation of the amplitude of static polar A_{2u} distortion $Q_{A_{2u}}$ induced by the electric field are shown with black solid and dashed lines for unstrained and strained structures, respectively. The red solid and dashed lines show the corresponding spin-splitting energy of the second-highest valence bands for the unstrained and strained structures. The inset shows the calculated electric polarization as a function of static A_{2u} distortions. (c) Energy well of $Q_{A_{2u}}$, for unstrained and 2% strained structures.

transform of the operators, viz., $b_k^\dagger = \frac{1}{\sqrt{N}} \sum_i e^{ik \cdot r_i} b_i^\dagger$, $b_k = \frac{1}{\sqrt{N}} \sum_i e^{-ik \cdot r_i} b_i$, and similarly for the operator $a_j^\dagger(a_j)$, we obtain Eq. (1) of the main text with the fol-

lowing forms A_k , B_k , and C_k in terms of the various exchange couplings J_i ($i = 1-7$):

$$A_k = 2J_1 [\cos(k_z c) - 1] + 8J_2 + 2J_3 [\cos(k_y a) + \cos(k_x a) - 2] + 2J_4 [\cos(k_z c + k_x a) + \cos(k_z c - k_x a) - 2] + 24J_5 + 2J_6 [\cos(k_z c) - 1] + 2J_7^a [\cos(k_y + k_x) a - 1] + 2J_7^b [\cos(k_y - k_x) a - 1] \quad (6)$$

$$B_k = 2J_1 [\cos(k_z c) - 1] + 8J_2 + 2J_3 [\cos(k_y a) + \cos(k_x a) - 2] + 2J_4 [\cos(k_z c + k_x a) + \cos(k_z c - k_x a) - 2] + 24J_5 + 2J_6 [\cos(k_z c) - 1] + 2J_7^a [\cos(k_y - k_x) a - 1] + 2J_7^b [\cos(k_y + k_x) a - 1] \quad (7)$$

and

$$C_k = C_k^* = 8 \cos\left(\frac{k_x a}{2}\right) \cos\left(\frac{k_y a}{2}\right) \cos\left(\frac{k_z c}{2}\right) \times \left[J_2 + J_5 \left(4 \left(\cos^2\left(\frac{k_x a}{2}\right) + \cos^2\left(\frac{k_y a}{2}\right) + \cos^2\left(\frac{k_z c}{2}\right) \right) - 9 \right) \right] \quad (8)$$

Here, a and c represent the tetragonal lattice constants of the MnF_2 unit cell. J_i denotes the exchange coupling between the i^{th} NNs of Mn atoms.

IV. EFFECTIVE MODEL

Symmetry adapted free energy expansion with $Q_{A_{1g}}$ and $Q_{A_{2u}}$ distortions is given by,

$$U \approx \alpha_1 Q_{A_{1g}}^2 + \alpha_2 Q_{A_{1g}}^4 + \beta_1 Q_{A_{2u}}^2 + \beta_2 Q_{A_{2u}}^4 + \lambda_1 Q_{A_{2u}}^2 Q_{A_{1g}} + \lambda_2 Q_{A_{2u}}^2 Q_{A_{1g}}^2 + O(Q^5) \quad (9)$$

We fit DFT energies to estimate the values of the coefficients in Eq. (9). We used a DFT training set of 40 different structures in the fitting process. These structures are

generated by condensing different combinations of $Q_{A_{2u}}$ and $Q_{A_{1g}}$. Optimal values of the Raman-active mode amplitude $Q_{A_{1g}}$ for fixed values of the polar distortion $Q_{A_{2u}}$ are estimated from Eq. (9) by setting $\frac{dU}{dQ_{A_{1g}}} = 0$. The obtained values of $Q_{A_{1g}}$, as depicted in Fig. 6a as a function of $Q_{A_{2u}}$, are close to the $Q_{A_{2u}} = Q_{A_{1g}}$ values.

Further, we estimate the required electric field to induce $Q_{A_{2u}}$ polar distortions by including an extra term $\Omega \mathcal{E}_z P_z$ in Eq. (9), as given below,

$$U \approx \alpha_1 Q_{A_{1g}}^2 + \alpha_2 Q_{A_{1g}}^4 + \beta_1 Q_{A_{2u}}^2 + \beta_2 Q_{A_{2u}}^4 + \lambda_1 Q_{A_{2u}}^2 Q_{A_{1g}} + \lambda_2 Q_{A_{2u}}^2 Q_{A_{1g}}^2 + O(Q^5) - \Omega \mathcal{E}_z P_z \quad (10)$$

Here, Ω , \mathcal{E}_z , P_z are respectively the volume of the unit

cell, applied electric field, and the electric polarization of the system along \hat{z} . Here, Ω is 82.748 \AA^3 . Further, we calculate the electric polarization of the structures at different amplitudes of $Q_{A_{2u}}$ polar distortions employing the Berry Phase method [92–94]. The electric polarization varies linearly with $Q_{A_{2u}}$, viz., $P_z = 0.785Q_{A_{2u}} \text{ C/m}^2$. Substituting P_z in Eq. (10) and solving the equation, we obtain the optimal value of \mathcal{E}_z required to generate a given amplitude of $Q_{A_{2u}}$ distortion, where we constraint $Q_{A_{2u}} = Q_{A_{1g}}$. The results of our calculations are shown in Fig. 6b, suggesting the possibility of achieving control over spin splitting with a reasonable external electric field [83–85].

Further, we consider the effect of compressive biaxial strain along the ab plane, which softens the A_{2u} phonon mode, and consequently reduces the magnitude of E_z , required to tune the spin splitting. Our phonon calculation

for the strained $P4_2/mnm$ structure with AFM configuration shows a reduction of 7.7% in the frequency of the A_{2u} phonon mode compared to the unstrained case. A softer A_{2u} distortion leads to a flatter energy well, as shown in Fig. 6c, resulting in a 4.5% reduction in the harmonic coefficient (β_1) compared to the unstrained case. With the new coefficient β_1 and assuming other parameters unchanged, we estimate \mathcal{E}_z from Eq. (10). Our calculation shows a reduction in the value of \mathcal{E}_z to induce a similar $Q_{A_{2u}}$ polar distortion amplitude, as shown in Fig. 6b. Although this is a rough estimation, and in principle, the effect of strain on the other parameters in Eq. (10) should also be considered, our calculations show that under bi-axial strain, the static combined $Q_{A_{2u}}$ and $Q_{A_{1g}}$ distortions lead to a modification of the spin splitting, which can now be achieved with a smaller applied electric field, as illustrated in Fig. 6b.